Ying *et al. Microstructures* 2023;3:2023018
DOI: 10.20517/microstructures.2022.47

Microstructures

Research Article

Open Access

Check for updates

Formation of strong and ductile FeNiCoCrB network-structured high-entropy alloys by fluxing

Huiqiang Ying[1,#], Xiao Yang[1,#], Haiyan He[2,#], Kairui Tao[1], Zheng Guo[1], Lifeng Wang[3], Jiacheng Ge[1], Sinan Liu[1], Shu Fu[1], Yu Lou[1], Lunhua He[4,5,6], Yang Ren[7], He Zhu[1], Zhenduo Wu[8,9], Si Lan[1]

[1]Herbert Gleiter Institute of Nanoscience, School of Materials Science and Engineering, Nanjing University of Science and Technology, Nanjing 210094, Jiangsu, China.
[2]School of Physical Sciences, Great Bay University, Dongguan 523000, Guangdong, China.
[3]Nanjing Huaxing Pressure Vessel Manufacture Co., Nanjing 210000, Jiangsu, China.
[4]Beijing National Laboratory for Condensed Matter Physics, Institute of Physics, Chinese Academy of Sciences, Beijing 100190, China.
[5]Spallation Neutron Source Science Center, Dongguan 523803, Guangdong, China.
[6]Songshan Lake Materials Laboratory, Dongguan 523808, Guangdong, China.
[7]Department of Physics, City University of Hong Kong, 83 Tat Chee Avenue, Kowloon, Hong Kong, China.
[8]City University of Hong Kong (Dongguan), Dongguan 523000, Guangdong, China.
[9]Center for Neutron Scattering, City University of Hong Kong Shenzhen Research Institute, Shenzhen 518057, Guangdong, China.
[#]Authors contributed equally.

Correspondence to: Prof. Zhenduo Wu, City University of Hong Kong (Dongguan), Dongguan 523000, Guangdong, China. E-mail: zd.wu@cityu.edu.cn; Prof. Si Lan, Herbert Gleiter Institute of Nanoscience, School of Materials Science and Engineering, Nanjing University of Science and Technology, Nanjing 210094, Jiangsu, China. E-mail: lansi@njust.edu.cn

How to cite this article: Ying H, Yang X, He H, Tao K, Guo Z, Wang L, Ge J, Liu S, Fu S, Lou Y, He L, Ren Y, Zhu H, Wu Z, Lan S. Formation of strong and ductile FeNiCoCrB network-structured high-entropy alloys by fluxing. *Microstructures* 2023;3:2023018. https://dx.doi.org/10.20517/microstructures.2022.47

Received: 30 Dec 2022 **First Decision:** 31 Jan 2023 **Revised:** 22 Feb 2023 **Accepted:** 3 Mar 2023 **Published:** 24 Mar 2023

Academic Editor: Huijun Li **Copy Editor:** Fangling Lan **Production Editor:** Fangling Lan

Abstract

A series of $[(FeNiCo)_{0.85}Cr_{0.15}]_{100-x}B_x$ (x = 12, 15, 17) high-entropy alloys with network-like microstructures (N-HEAs) and a wavelength of 3-5 μm was prepared using the fluxing method. The novel N-HEAs exhibited higher strength and ductility compared with samples obtained by suction casting. Neutron diffraction and scanning electron microscopy measurements showed that the network-like structure contained soft face-centered cubic (FCC) and hard tetragonal Cr_2B-type sub-networks. The network-like structure was formed during the solidification of the molten alloy from a deeply undercooled state, achieved by removing impurities and most metallic oxides through B_2O_3 fluxing. The mechanical properties could be tuned by modifying the composition to change the volume fractions of the different sub-networks. When x decreased from 17 to 12, the compressive yield strength decreased from 1.6 to 1.1 GPa, while the compressive strain increased from ~20% to ~70%. The N-HEA samples with x = 12

© The Author(s) 2023. **Open Access** This article is licensed under a Creative Commons Attribution 4.0 International License (https://creativecommons.org/licenses/by/4.0/), which permits unrestricted use, sharing, adaptation, distribution and reproduction in any medium or format, for any purpose, even commercially, as long as you give appropriate credit to the original author(s) and the source, provide a link to the Creative Commons license, and indicate if changes were made.

and 15 also exhibited a good tensile ductility of 19% and 14%, respectively. *In situ* synchrotron X-ray diffraction results revealed an inhomogeneous deformation behavior, i.e., the soft FCC phase yielded prior to the hard Cr_2B-type phase, which bore more stress in the initial stage of the plastic deformation. In the later stage of the plastic deformation, the ductility of the sample was provided by the FCC phase, together with some contributions from the Cr_2B-type phase.

Keywords: Network-structured high-entropy alloys, neutron and X-ray diffraction, mechanical properties, fluxing method

INTRODUCTION

High-entropy alloys (HEAs) or multi-principal-element alloys are a new class of structural materials that have attracted widespread attention since their first synthesis in 2004[1-3]. The development of HEAs provided a new strategy for alloy design, leading to the discovery of new alloys with superior properties in a wide range of loading conditions[4,5]. By tuning the composition, various researchers have developed HEAs with exceptional ductility and fracture toughness at temperatures down to 20 K[6-8], as well as strong and ductile mechanical behavior from cryogenic temperatures to 1073 K[9], and excellent soft magnetic properties with high strength and ductility[10]. Moreover, the nanoscale structural design has been applied to further increase the strength and ductility of HEAs by introducing nanoscale precipitation[11], compositional modulation[12], or disordered grain boundaries[13]. However, these heterogeneous nanostructures may be unstable at elevated temperatures or difficult to fabricate in bulk sizes[14,15], which limits their industrial application. On the other hand, at a larger (i.e., sub-micron to micron) scale, the structure of the HEAs could also significantly influence their mechanical properties, as in the case of lamellar structures[16] or equiaxed grains[17]. These structures could be controlled by conventional thermal/mechanical treatments, i.e., cold/hot rolling or annealing[18-20]. Thus, developing new structures at the sub-micron to micron scale by engineering-friendly methods could be a promising way to accelerate the application of HEAs.

The fluxing technique is a widely used heat treatment method in metallurgy, in which the impurity and metallic oxide contents of the molten alloy are reduced by immersing in molten oxides[21] or salts[22] to improve its properties. This approach has been successfully applied to achieve a large undercooling of different alloy melts, in order to alter the solidification kinetics[23,24] or even form bulk metallic glasses[21]. Novel microstructures could be formed when the melt is solidified at a deeply undercooled state by fluxing, which is difficult to reach with other techniques. For example, using the B_2O_3 fluxing treatment, Fe-C and Fe-B-C alloys can be cast into an interconnected network morphology at the submicron to micron scale, showing higher strength and plasticity than white cast iron with a typical eutectic structure[25].

In this work, the B_2O_3 fluxing treatment was applied to fabricate high-entropy alloys with novel network-like microstructures (N-HEAs)[26,27]. A high degree of undercooling (385 K) was achieved for $[(FeNiCo)_{0.85}Cr_{0.15}]_{100-x}B_x$ (x = 12, 15, 17) N-HEAs with a diameter of ~13 mm. The morphology of the microstructures was inspected by scanning electron microscopy (SEM) and transmission electron microscopy (TEM), and the phase composition was studied by energy-dispersive spectroscopy (EDS) and neutron diffraction. The deformation mechanism was further investigated using *in situ* synchrotron X-ray diffraction during tension test. We also discuss the origin of the large undercooling, the relationship of the mechanical properties with the microstructures, as well as phase fractions, and the deformation mechanism.

MATERIALS AND METHODS

Sample preparation and fluxing treatment

$[(FeNiCo)_{0.85}Cr_{0.15}]_{100-x}B_x$ (x = 12, 15, 17) ingots were prepared by vacuum induction heating using pure elements (purity > 99.95 wt.%). Then, the alloy ingots were remelted at least five times under a high-purity Ti-gettered argon atmosphere in a water-cooled copper crucible; the ingots were flipped each time to improve the chemical homogeneity. After that, the alloy ingots were transferred into molten B_2O_3 and underwent fluxing treatment for 2 h at 1,473 K in a dry-cleaned fused silica tube with inner and outer diameters of 16 and 19 mm, respectively. A schematic diagram of the fluxing experiment setup is shown in Figure 1A. After the fluxing treatment, the fused silica tube was removed from the muffle furnace and cooled in air. A high-speed camera and a thermocouple[28] were used to record the cooling process of the system and the temperature history, respectively. To measure the liquidus temperature (T_L) of the samples, differential scanning calorimeter (DSC) experiments (Netzsch 404 F3) were performed under a high-purity argon atmosphere, with a cooling rate of 20 K min^{-1} from 1,500 K to 300 K.

Neutron and synchrotron X-ray diffraction experiments

Time-of-flight neutron diffraction experiments in transmission mode were carried out on the General Purpose Powder Diffractometer (GPPD) beamline at the China Spallation Neutron Source[29], with a neutron beam bandwidth and size of 4.5 Å and 40 × 20 mm, respectively. Diffraction data were collected for 2 h on each sample. The microstructure was determined by Rietveld refinement using the GSAS software[30]. *In situ* high-energy synchrotron X-ray diffraction measurements were performed at the 11-ID-C beamline of the Advanced Photon Source (APS, Argonne National Laboratory). High-energy X-rays with a wavelength of 0.01173 nm were used for data collection. The strain rate used in the *in situ* tensile test is 4×10^{-4} s^{-1}. The lattice strain ε_{hkl} was calculated as $(d_{hkl} - d^{\circ}_{hkl})/(d^{\circ}_{hkl})$, where d_{hkl} is the lattice spacing of the hkl planes, and d°_{hkl} is the corresponding value for the stress-free sample[6].

Morphology characterization and mechanical tests

The morphology and composition of the alloy were characterized using FEI Quanta 250F SEM, JSM-IT500HR SEM, and FEI Talos F200X TEM microscopes equipped with an attached X-ray EDS instrument. Cylinder-shaped compressive samples with a diameter of 3 mm and a height of 4.5 mm, as well as dog-bone-shaped tensile specimens with a gauge length of 10 mm and a thickness of 1mm were fabricated by electrical discharge machining. To obtain the tensile specimens, the spherical fluxed ingots were subjected to an additional treatment, consisting of annealing at 1,273 K for 10 h, hot rolling (with 80% thickness reduction), and annealing at 1,273 K for 10 h again. Uniaxial compressive and tensile tests were performed on a UTM4304GD testing machine with a strain rate of 1×10^{-3} s^{-1}. Hardness values were measured with a HVST-1000Z (Deka Precision Measuring Instrument) tester.

RESULTS

Measurement of degree of undercooling achieved by fluxing treatment

Figure 1B shows the solidification process of the $[(FeNiCo)_{0.85}Cr_{0.15}]_{83}B_{17}$ alloy melt immersed in molten B_2O_3. The photographs in Figure 1B display the cooling process of the molten alloy ingot. After air-cooling for 35 s 14 ms, recalescence occurred due to latent heat released during crystallization[31]. The crystallization occurred on the sample surface, and the crystal/liquid interface gradually moved across the whole sample within 5 ms. Figure 1C shows the temperature changes during the cooling process, as recorded by the thermocouple. At the beginning of the process, the sample was air-cooled with an average cooling rate of 2 K s^{-1}. The temperature increased by 135 K during recalescence, as marked by the red arrow in Figure 1C. The liquidus temperature of the $[(FeNiCo)_{0.85}Cr_{0.15}]_{83}B_{17}$ N-HEA was measured to be 1,350 K [Figure 1D]. Thus, the undercooling of the molten alloys with a diameter of approximately 13 mm could be estimated at 385 K. The DSC curves of $[(FeNiCo)_{0.85}Cr_{0.15}]_{85}B_{15}$ and $[(FeNiCo)_{0.85}Cr_{0.15}]_{88}B_{12}$ N-HEAs are also shown in

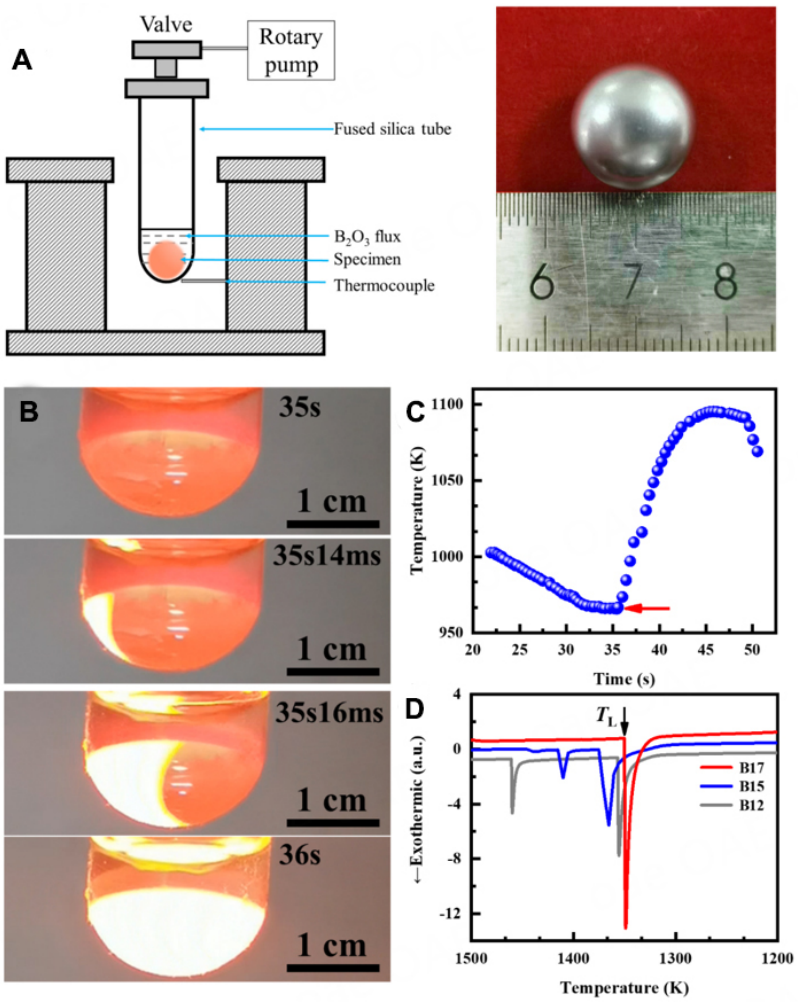

Figure 1. (A) Schematic diagram of B_2O_3 fluxing experiment setup (left). Photograph of alloy ingot showing the morphology of the specimen after fluxing (units: cm) (right). (B) Solidification process of molten alloy droplet, showing the recalescence phenomenon. (C) Cooling curve of $[(FeNiCo)_{0.85}Cr_{0.15}]_{83}B_{17}$ N-HEA melt. The red arrow indicates the occurrence of recalescence. (D) DSC curves of $[(FeNiCo)_{0.85}Cr_{0.15}]_{100-x}B_x$ (x = 12, 15, 17) N-HEAs during cooling process. The black arrow indicates the liquidus temperature of $[(FeNiCo)_{0.85}Cr_{0.15}]_{83}B_{17}$ N-HEA.

Figure 1D for comparison.

Neutron diffraction measurements and phase identification

The neutron diffraction patterns of the fluxed N-HEAs are shown in Figure 2A-C. Because of the neutron absorption of the B element, samples were polished to a thickness of ~200 μm to increase the transmittance. Vanadium boxes were used as sample holders; hence, the diffraction spectrum of the vanadium background could also be observed. Rietveld refinement of the neutron diffraction patterns revealed that the fluxed N-HEAs contained a tetragonal Cr_2B-type intermetallic phase and an FCC solid solution. The lattice parameter of the FCC solid solution was 3.5643 Å, while the parameters of the Cr_2B-type intermetallic phase were $a = b = 5.0926$ Å, $c = 4.2237$ Å, and $\alpha = \beta = \gamma = 90°$. For the sample with $x = 17$, the fraction of the Cr_2B-type phase was 61 wt.%, larger than that of the FCC phase, 39 wt.%. When the B content decreased to 12%, the fraction of Cr_2B-type phase dropped to 55 wt.%, and the FCC phase fraction increased to 45 wt.%. For the sample with $x = 15$, the phase fractions lay between the above values. Image processing based on the CAD software was employed to calculate the volume fraction of the two phases, according to the contrast

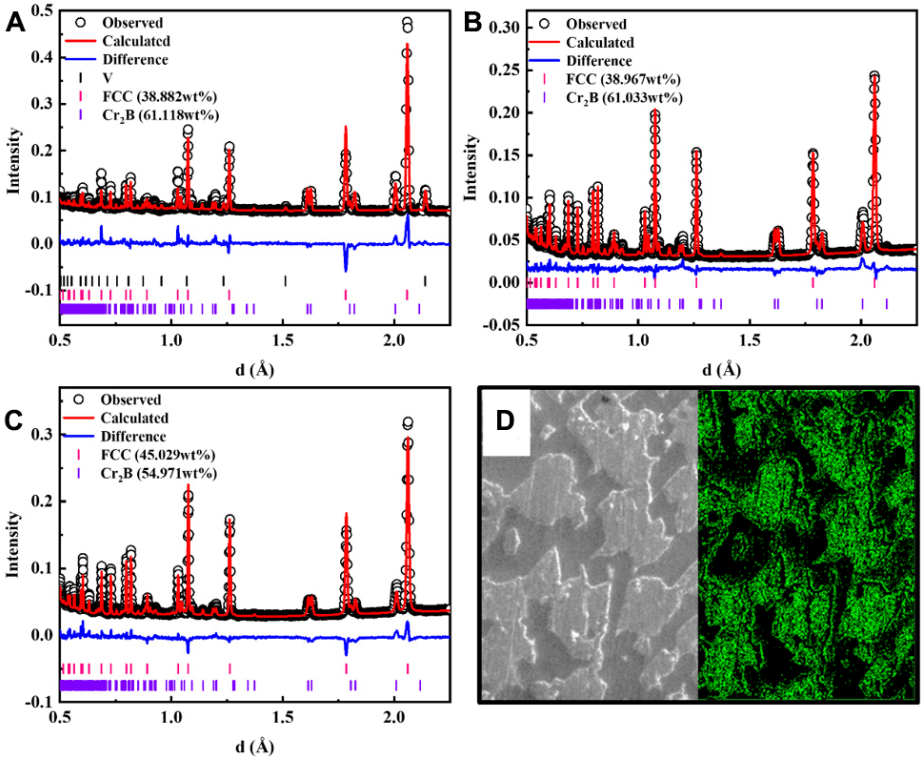

Figure 2. Neutron diffraction patterns and Rietveld refinement results of the fluxed $[(FeNiCo)_{0.85}Cr_{0.15}]_{100-x}B_x$ N-HEAs, with x = 17 (A), 15 (B), and 12 (C). (D) Illustration of image processing approach used to estimate the phase fractions; the left half shows the SEM image, and the right half displays the processed image used to calculate the phase fraction.

difference between different phases in SEM images of the samples (details of the phase identification from the SEM images are presented in Section "Network-like morphology of fluxed N-HEA samples"); the results are illustrated in Figure 2D, which is consistent with the data obtained from neutron diffraction.

Network-like morphology of fluxed N-HEA samples

Figure 3A-D show SEM images of the $[(FeNiCo)_{0.85}Cr_{0.15}]_{100-x}B_x$ (x = 12, 15, 17) N-HEAs. Figure 3A displays the SEM image of the non-fluxed suction-cast $[(FeNiCo)_{0.85}Cr_{0.15}]_{83}B_{17}$ N-HEA, showing coarse and elongated dendrites with sizes above 10 μm[32]. However, as shown in Figure 3B, the fluxed N-HEAs possessed a uniform network-like morphology, consisting of dark (zone A) and bright (zone B) sub-networks. The wavelength of the network structure was around 3-5 μm, thus smaller than the size of the dendrites in the non-fluxed sample. When the B content changed from 12% to 17%, the volume fraction of the dark phase (zone A) showed a gradual increase [Figure 3B-D]. For samples with x < 12%, the network structure may be further broken because the volume fraction of the dark phase is too small to be well interconnected.

Figure 4A and B show the elemental distributions of zones A and B determined by SEM/EDS mapping analysis of the $[(FeNiCo)_{0.85}Cr_{0.15}]_{83}B_{17}$ HEA. Zone A was found to be Cr-rich, whereas zone B was Ni-rich. Even though the non-fluxed sample had a different morphology, its elemental distribution was similar to the fluxed samples, with the brighter part containing more Ni. Because of its low atomic number, the B element is too light to be detected by EDS, and the corresponding data are not accurate in Figure 4. The results for the fluxed $[(FeNiCo)_{0.85}Cr_{0.15}]_{85}B_{15}$ and $[(FeNiCo)_{0.85}Cr_{0.15}]_{88}B_{12}$ samples were consistent with those obtained for $[(FeNiCo)_{0.85}Cr_{0.15}]_{83}B_{17}$. The TEM/EDS mapping results of the fluxed $[(FeNiCo)_{0.85}Cr_{0.15}]_{83}B_{17}$

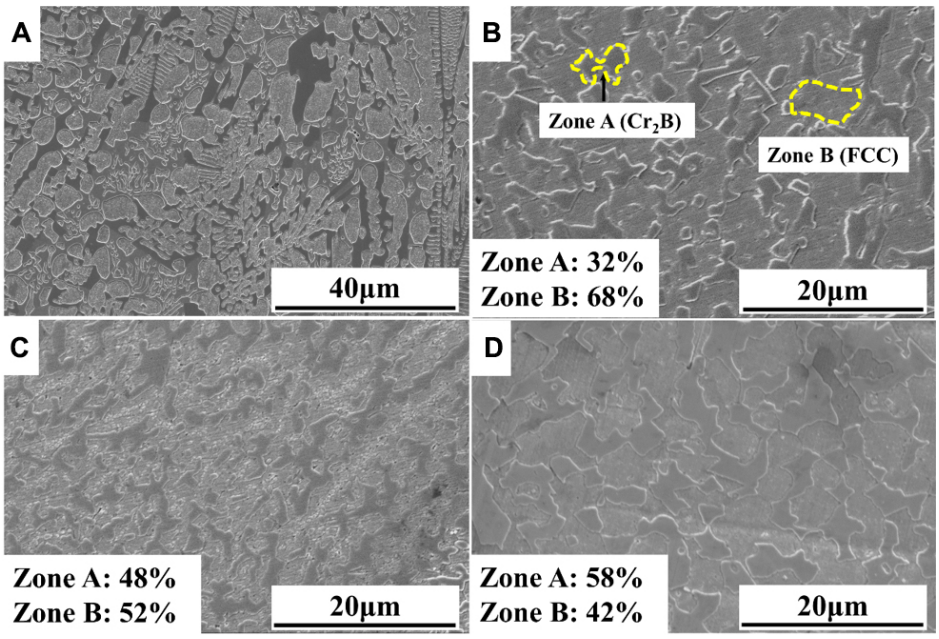

Figure 3. SEM images showing morphology of bulk $[(FeNiCo)_{0.85}Cr_{0.15}]_{100-x}B_x$ (x = 12, 15, 17) N-HEAs prepared by suction casting after arc melting for x = 17 (A), and by the fluxing method for x = 12 (B), x = 15 (C), and x = 17 (D). The phase fractions obtained by SEM image processing are superimposed in the figures for direct comparison.

sample are also shown in Figure 4C. The selected-area electron diffraction patterns displayed in the insets of the bright-field TEM image in Figure 4C show the phase information of each network. The elemental distribution of both networks was consistent with that obtained by SEM/EDS. As the TEM/EDS results may be more accurate than SEM/EDS, the compositions of zone A and zone B obtained with this approach are summarized in Table 1.

Mechanical properties of fluxed samples with different B contents

Figure 5A shows the compressive stress-strain curves of the fluxed $[(FeNiCo)_{0.85}Cr_{0.15}]_{100-x}B_x$ (x = 12, 15, 17) N-HEAs. As a reference, the figure also shows the data of the non-fluxed suction-cast $[(FeNiCo)_{0.85}Cr_{0.15}]_{83}B_{17}$ N-HEA, which exhibited a brittle fracture behavior, with an ultimate strength of 2.3 GPa. The fluxed N-HEAs, with a uniform network-like structure, showed an excellent combination of strength and plasticity. The yield strength and compressive strain of the sample with x = 17 (denoted as B17) were 1.6 GPa and 20%, respectively, whereas those of the sample with x = 12 (denoted as B12) were 1.1 GPa and > 70%, respectively. The mechanical properties of the sample with x = 15 (B15) were intermediate between those of the B17 and B12 samples. Because of its significant plasticity, the B12 sample did not break up during the compression test. In addition, the fluxed N-HEAs showed work-hardening behavior, as illustrated by the corresponding rate curves in Figure 5B. In particular, the tensile ductility of the B12 and B15 samples reached 19% and 14%, respectively [Figure 5C]. Because of the dual-phase structure and hot rolling treatment for tensile specimens, there is a tension-compression asymmetry of B12 and B15 samples. The yield strength, compressive strain, and hardness data are summarized in Figure 5D, which shows a good correlation of these parameters with the B content and volume fractions of the constituent phases.

Deformation mechanism revealed by *in situ* synchrotron X-ray diffraction

Figure 6A shows the synchrotron X-ray diffraction patterns of the $[(FeNiCo)_{0.85}Cr_{0.15}]_{88}B_{12}$ sample at different deformation stages along the loading direction. The enlarged view shows the changes in peak position and intensity, as well as the broadening of the peak profile during deformation. The lattice strains of the

Table 1. Chemical compositions of zone A and zone B estimated from TEM/EDS (at. %)

Element concentration (at. %)	Fe	Ni	Co	Cr	B
Zone A (dark region in Figure 4B)	26.47	10.33	26.87	35.08	1.25
Zone B (bright region in Figure 4B)	27.85	36.46	29.84	5.84	0.01

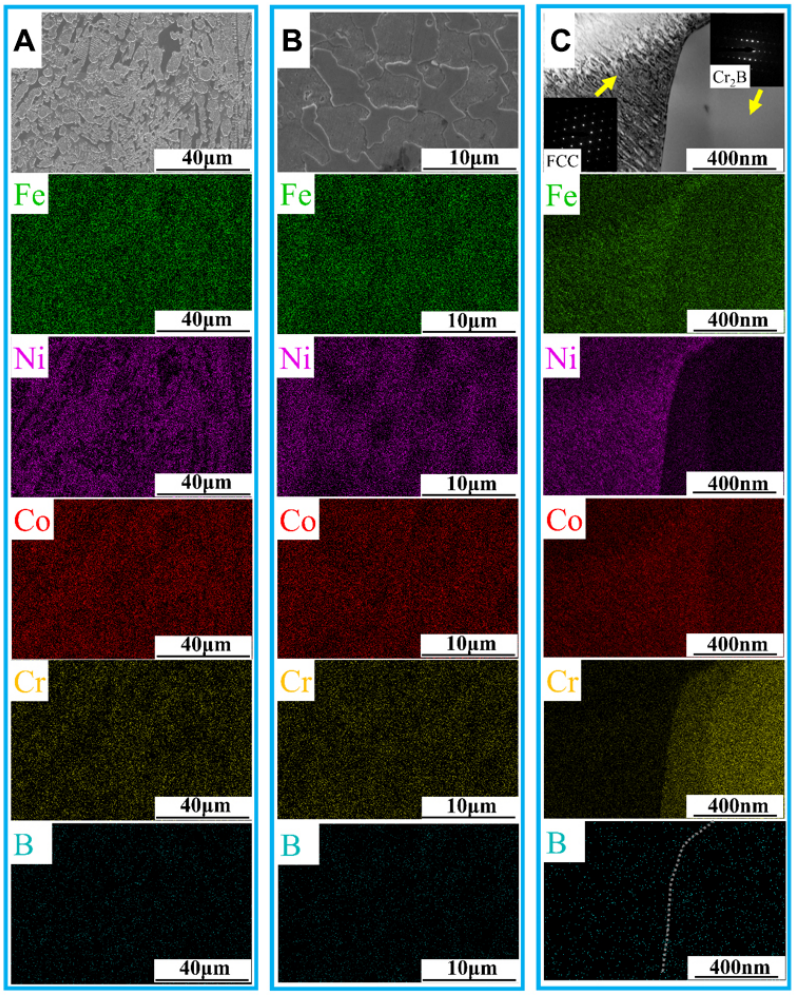

Figure 4. SEM/EDS mapping results for the non-fluxed suction-cast (A) and fluxed (B) $[(FeNiCo)_{0.85}Cr_{0.15}]_{83}B_{17}$ N-HEAs, showing Zone A (Cr_2B) is Cr-rich and Zone B (FCC) is Ni-rich. (C) TEM/EDS mapping results for the fluxed $[(FeNiCo)_{0.85}Cr_{0.15}])_{83}B_{17}$ N-HEA. The upper picture of (C) is the TEM bright field image, showing the Cr_2B grain (right part) and the FCC grain (left part with moire fringes). The insets display the selected area electron diffraction patterns of each phase. The dashed line in the B element map of (C) denotes the grain boundary.

different phases were derived from the position shifts[6] of different Bragg peaks, and the results are shown in Figure 6B. According to the yielding of the different phases, the whole deformation could be divided into three regions. In the elastic region I (below 350 MPa), the lattice strain for all orientations changes linearly with the applied stress. The different slopes are a result of elastic anisotropy[33]. For the FCC phase, the (200) grains exhibited the largest lattice strain, while the (111) and (222) ones showed the smallest values. For the Cr_2B-type phase, the (002) grains displayed the largest lattice strain, followed by the (112) and (202) planes. Table 2 summarizes the grain orientation dependence of the elastic moduli (E_{hkl}), obtained from the slope of the linear relationship of stress and strain in the elastic region. In the FCC phase, (200) and (111) were the

Table 2. Elastic moduli of different (hkl) planes in FCC and Cr_2B-type phases

FCC phase				Cr_2B-type phase		
E_{111}/GPa	E_{200}/GPa	E_{220}/GPa	E_{311}/GPa	E_{002}/GPa	E_{112}/GPa	E_{202}/GPa
244 ± 7	160 ± 4	222 ± 8	197 ± 2	168 ± 4	190 ± 4	229 ± 8

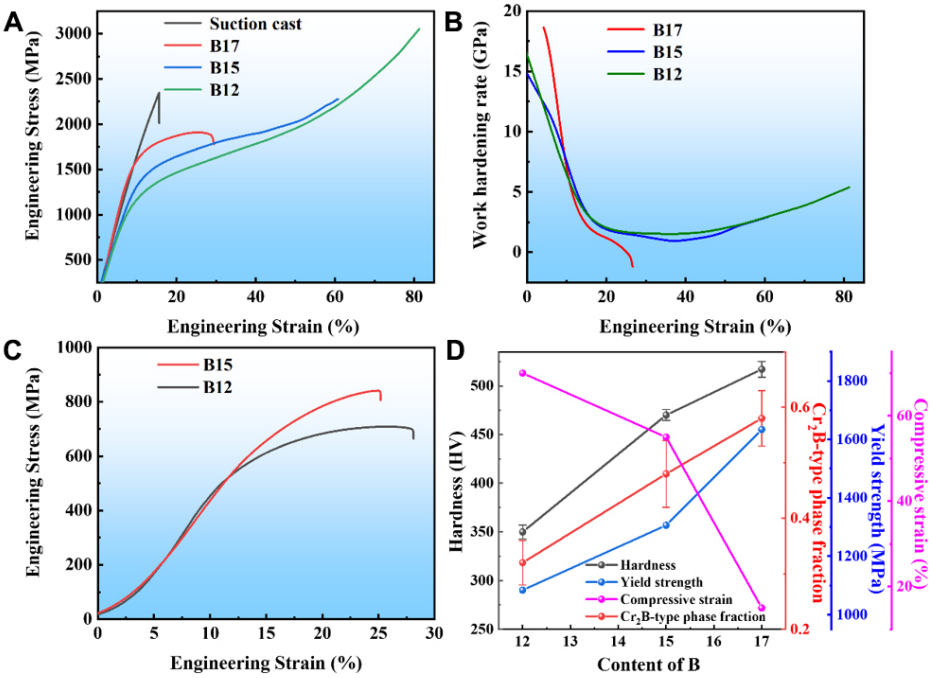

Figure 5. (A) Engineering compressive stress-strain curves of $[(FeNiCo)_{0.85}Cr_{0.15}]_{100-x}B_x$ (x = 12, 15, 17) N-HEAs. (B) Work-hardening rate curves for fluxed samples. (C) Tensile stress-strain curves of fluxed B12 and B15 samples. (D) Evolution of mechanical properties of $[(FeNiCo)_{0.85}Cr_{0.15}]_{100-x}B_x$ N-HEAs as a function of B content.

elastically softest and stiffest orientations, respectively, similar to other FCC alloys[34,35]. In the Cr_2B-type phase, the (002) orientation was more compliant compared with the (112) and (202) ones. Above 350 MPa (region II), the lattice strains for all FCC grains lost their linear relationship and stopped increasing with the applied stress, indicating that the FCC phase yielded. The plastic deformation of the soft FCC phase was constrained by the hard Cr_2B-type phase, as no macroscopic yielding could be observed. In contrast, the lattice strains of the Cr_2B-type phase increased more rapidly. When the stress increased to around 500 MPa (region III), the Cr_2B-type phase started to deform plastically, as evidenced by the deviation from the linearity of the (112) and (202) planes. Moreover, the lattice strain of the Cr_2B-type phase in regions II and III was generally larger than that of the FCC phase, showing that the Cr_2B-type phase bore more stress in the plastic regime; this indicates the existence of stress partitioning among the different phases[36,37]. Another feature worth noting is the absence of splitting between the lattice strains of the (111) and (222) planes in the FCC phase, suggesting that no stacking fault was formed during deformation[38].

The evolution of the normalized peak intensity, representing the texture development, is shown in Figure 6C for both the FCC and Cr_2B-type phases. In the case of the FCC phase, no noticeable texture was observed in region I. After yielding (regions II and III), the normalized intensity of the (111) and (222) peaks increased, while that of the (220) decreased. These intensity changes result from the characteristic texture caused by dislocation slip in FCC alloys[39-42]. Combined with the lattice strain evolution results, we

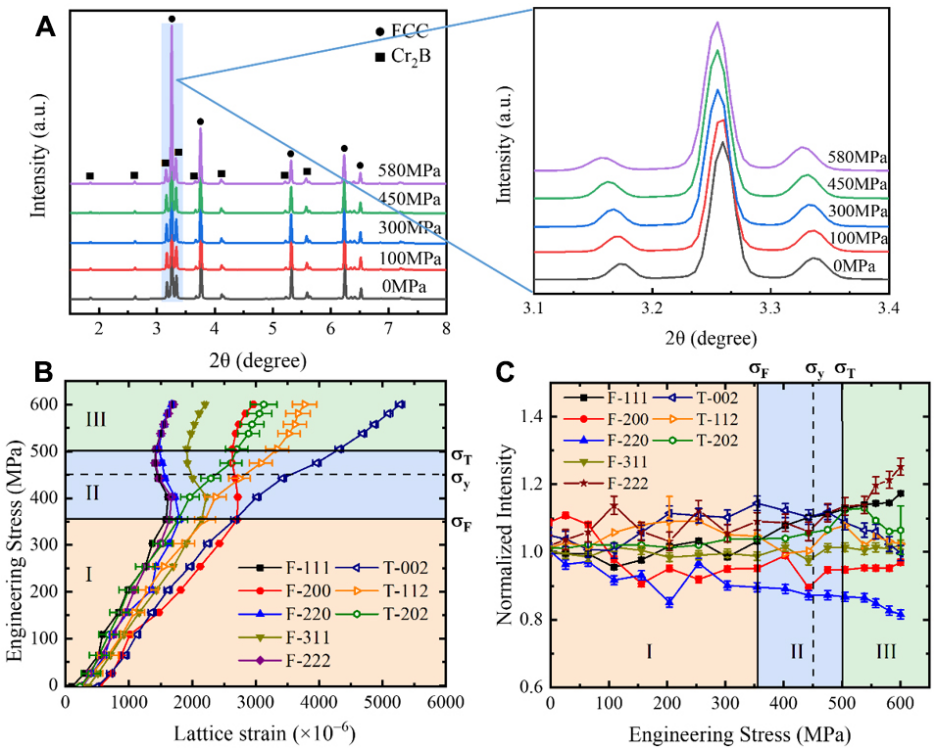

Figure 6. (A) Synchrotron X-ray diffraction patterns of $[(FeNiCo)_{0.85}Cr_{0.15}]_{88}B_{12}$ sample along the loading direction at different deformation stages. The inset shows an enlarged view of the evolution of the main peaks. (B) Relationship of lattice strain of FCC and Cr_2B-type phases with engineering stress. (C) Texture development (represented by the normalized integrated intensity of different Bragg peaks) in FCC and Cr_2B-type phases with engineering stress. For clarity, error bars are only shown for selected points on (112) and (202) reflections. F and T denote the FCC and tetragonal Cr_2B-type phases, respectively.

can conclude that dislocation slip was the main deformation mechanism for the FCC phase. However, no distinct texture was formed in the Cr_2B-type phase.

DISCUSSION

Origin of large degree of undercooling

The as-prepared fluxed N-HEAs showed high strength and ductility. One of the key requirements for forming a network-like structure at the submicron to micron scale is that the deep undercooled liquid state should be accessible before crystallization[25]. In this work, the degree of undercooling in the centimeter-sized B17 N-HEAs could reach values as high as 385 K, showing the great application potential of this alloy. The fluxing agent B_2O_3 plays an essential role in reducing the contents of impurities and surface metallic oxides in the sample, increasing the undercooling degree[21]. On the other hand, various degrees of chemical short-range order can coexist in the molten alloys, due to the complex composition of HEAs[43], which hinders crystallization during undercooling[44,45]. These two mechanisms could explain the large undercooling of the N-HEAs.

Formation of network morphology in fluxed N-HEAs

One of the possible mechanisms of network structure formation is spinodal decomposition. A liquid-state miscibility gap may exist in the undercooled liquids of metal-metalloid alloy systems (i.e., Fe-B, Fe-B-C), due to the existence of unique short-range orders in the undercooled liquids[24,28,46]. The chemical complexity of the undercooled HEA liquids studied here would facilitate the formation of short-range order[43], potentially enabling the formation of a metastable miscibility gap. Once sufficient undercooling is reached,

the HEA liquids may transform into network liquids through spinodal decomposition[47]. The solidification of the spinodal network liquids then results in the formation of a crystalline network structure. Moreover, other mechanisms may also be factors of network structure. Literature[48-50] showed that the Rayleigh instability may induce the fragmentation of dendrites during recalescence at large undercooling, resulting in a network structure. Furthermore, another factor is the entropy effect. With increasing configurational entropy, the growth morphology may transit from dendritic to faceted[51,52], leading to a structure that is different from the dendritic[32,53], lamellar[54], or equiaxed grain structures[55,56] formed through conventional casting processes. Using conventional methods, the microstructures can only be modified in the solid state by thermal/mechanical treatments to introduce precipitates, structural defects, or refinement of the as-cast grains[55,57]. The fluxing technique offers a unique route to directly develop the network structure in bulk-sized samples through the solidification of undercooled liquids, highlighting the promising potential of the fluxed N-HEAs in industrial applications.

Composition dependence of phase fractions

The present results showed that the network-like structure could be controlled by tuning the B content of the alloys. The EDS results summarized in Table 1 show little difference between the Fe and Co contents in the two phases, while the Ni and Cr contents were significantly different. The enthalpy of mixing (ΔH) between elements is summarized in Table 3[58], which shows that the absolute ΔH value between Cr and B was the largest. Thus, it is reasonable that Cr and B prefer to segregate to form intermetallic phases in one sub-network. This was also confirmed by the neutron diffraction results, which revealed the presence of Cr_2B-type intermetallic phases. As long as the Cr element is still present in the FCC solid solution, the volume fraction of Cr_2B may increase with increasing B content.

Structural origin of improved mechanical properties

As summarized in Figure 5D, the mechanical behavior is correlated with the volume fractions of the soft/ductile FCC phase and hard/brittle Cr_2B-type intermetallic phase. The samples with a lower volume fraction of hard/brittle Cr_2B intermetallic phase exhibit a lower hardness and yield strength but a higher compressive strain. *In situ* synchrotron X-ray diffraction measurements of the tensile behavior of the B12 alloy revealed a three-stage deformation process, with the ductile FCC phase yielding earlier, and the hard Cr_2B-type intermetallic phase yielding later than the macroscopic yielding in the plastic region. The whole deformation is inhomogeneous, indicating that the deformation is accommodated between the two phases, maintaining the plastic compatibility. This heterogeneous deformation has also been observed in austenite-ferrite dual-phase steels[59,60]. The Cr_2B-type intermetallic phase bears more stress after yielding, as evidenced by the larger lattice strain. Similar to multiphase steel, where the hard phases bearing more stress ensure a sufficient work-hardening capability[37], the hard Cr_2B-type phase in the B12 alloy may contribute to a strain-hardening effect and an excellent combination of strength and ductility. Moreover, the FCC phase also has high work hardening ability due to the multiple slip systems as well as other deformation mechanisms such as stacking fault, twinning and phase transformation[6,39]. In this study, dislocations could be observed, as revealed by the increasing trend of F-111 and F-222 intensity in the plastic region, and no evidence of the involving stacking faults and phase transformation could be found from the synchrotron experiments. Further investigation is needed to explain the work-hardening effect of the FCC phase at a large strain.

In addition, although our *in situ* loaded sample only deformed to several percent, a tiny increase of lattice strain in the FCC phase after 500 MPa could be observed, which means that stress was partitioned with the FCC phase[61]. A previous study of austenite-martensite dual-phase steel attributed the improved ductility to stress transfer from the hard to the soft phase, forcing the two phases to deform together[33]. The cooperative deformation, as well as stress partitioning, could inhibit the strain localization and thus delay

Table 3. ΔH values (kJ/mol) between elements calculated by Miedema's model[58]

Elements	Fe	Ni	Co	Cr	B
Fe	/	-2	-1	-1	-26
Ni	-2	/	0	-7	-24
Co	-1	0	/	-4	-24
Cr	-1	-7	-4	/	-31
B	-26	-24	-24	-31	/

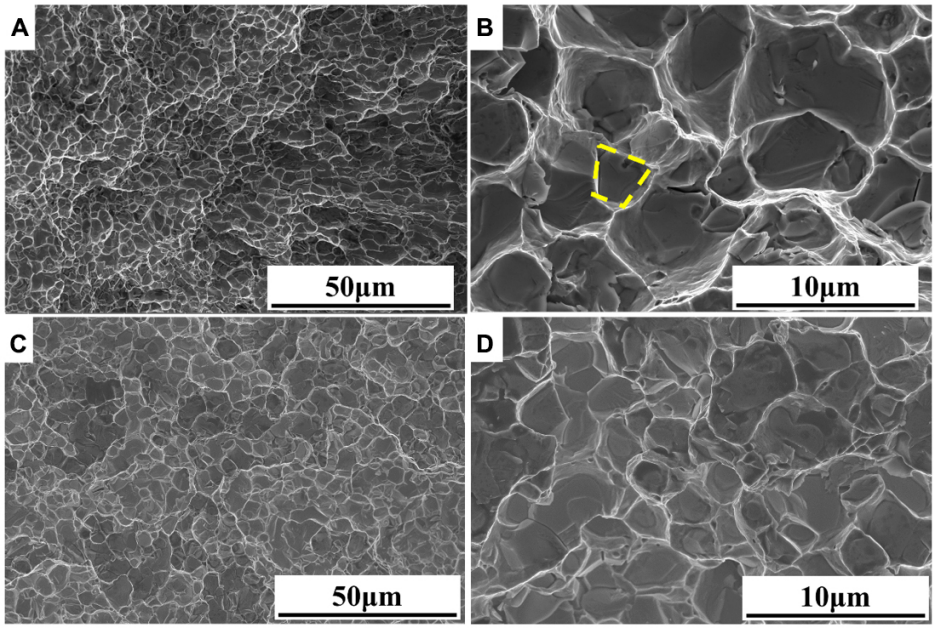

Figure 7. Fracture surface of B12 (A and B) and B15 (C and D) tensile samples, displayed at different magnifications.

the crack activation. Similar to this phenomenon, the enhanced combination of strength and ductility in the B12 alloy can be correlated to the dual-phase structure, where the hard Cr_2B-type intermetallic phase and the soft FCC phase deform synergically.

Figure 7 shows SEM images of the fracture surface of B12 obtained after the tensile test (the fracture surface of the B15 sample, i.e., Figure 7C and D, is similar). As shown in Figure 7A, the fracture surface contained uniformly distributed dimples, a typical fracture morphology for ductile samples[62]. The size of the dimples was about 3-5 μm, similar to the wavelength of a network structure. Furthermore, no large micro-voids were found on the fracture surfaces. Previous studies showed that 304 L austenitic stainless steels[63] and CrFeCoNi HEAs[62] with small-size dimples had high ductility. Our results indicate that the soft FCC phase may participate in the deformation process in stages involving large plastic deformations, contributing to improved ductility. The enlarged view of the fracture surface [Figure 7B] also displays some fracture patterns with sharp angles (marked by yellow lines), similar to the intergranular fracture surface of brittle samples[64]. This may be attributed to the deformation of the Cr_2B-type phase.

CONCLUSION

In this work, a series of $[(FeNiCo)_{0.85}Cr_{0.15}]_{100-x}B_x$ (x = 12, 15, 17) N-HEAs combining high strength and plasticity were successfully synthesized by the B_2O_3 fluxing technique. We used a set of advanced

characterization techniques to understand the structure and properties of these alloys. The conclusions are summarized below:

(1) The B_2O_3 fluxing treatment achieved a large degree of undercooling (385 K) of the centimeter-size N-HEAs alloy melts.

(2) The fluxed N-HEAs had a network-like structure with a wavelength of 3-5 μm; one sub-network consisted of a hard Cr_2B-type intermetallic phase, while the other was a soft FCC solid solution.

(3) The volume fraction of the two sub-networks could be tailored by varying the B concentration, resulting in a gradual change in the yield strength and compressive strain of the N-HEAs. When the B content decreased from 17% to 12%, the yield strength decreased from 1.6 to 1.1 GPa and the compressive strain increased from 20% to 70%.

(4) N-HEAs with B contents of 12% and 15% further exhibited a good tensile ductility of 19% and 14%, respectively. The *in situ* synchrotron X-ray diffraction analysis of the tensile behavior demonstrated that the whole deformation process could be divided into three regions based on the lattice strain evolution. This heterogeneous deformation originated from the strength difference between the two phases. Dynamic stress partitioning between the soft FCC phase and the hard Cr_2B-type intermetallic phases induced a cooperative deformation, which improved the ductility.

This work provides an industry-friendly route to fabricate N-HEAs with superior and controllable mechanical properties. Moreover, microalloying and thermal/mechanical treatment could be employed to further develop fluxed N-HEAs with excellent strength and ductility.

DECLARATIONS

Acknowledgements

We acknowledge Ms. Weixia Dong for her help in DSC measurements. This research used the resources of the Advanced Photon Source, a US Department of Energy (DOE) Office of Science User Facility operated for the DOE Office of Science by Argonne National Laboratory (No. DE-AC02-06CH11357). We acknowledge the support of the GPPD beamline of China Spallation Neutron Source (CSNS) in providing neutron diffraction research facilities.

Authors' contributions

Design: Lan S, Wu Z
Experiments and data collection: Yang X, Tao K, Guo Z, Wang L, Fu S, Lou Y, Ren Y, He L
Data analysis: Ying H, He H, Liu S, Ge J, Zhu H
Manuscript writing: Ying H, He H, Lan S, Wu Z
Manuscript revision and supervising: Lan S, Wu Z
All authors have read and agreed to the published version of the manuscript.

Availability of data and materials

The data that support the findings of this study are available from the corresponding author upon reasonable request.

Financial support and sponsorship

This work was financially supported by the National Key R&D Program of China (No. 2021YFB3802800), the National Natural Science Foundation of China (Nos. 51871120, 52222104, 52201190, and 12261160364), the Natural Science Foundation of Jiangsu Province (No. BK20200019), and Shenzhen Fundamental Research Program (No. JCYJ20200109105618137). Z.-D. Wu and S. Lan acknowledge the support of the Guangdong-Hong Kong-Macao Joint Laboratory for Neutron Scattering Science and Technology.

Conflicts of interest

All authors declared that there are no conflicts of interest.

Ethical approval and consent to participate

Not applicable.

Copyright

© The Author(s) 2023.

REFERENCES

1. Zhang Y, Zuo TT, Tang Z, et al. Microstructures and properties of high-entropy alloys. *Prog Mater Sci* 2014;61:1-93. DOI
2. Yeh J, Chen S, Lin S, et al. Nanostructured high-entropy alloys with multiple principal elements: novel alloy design concepts and outcomes. *Adv Eng Mater* 2004;6:299-303. DOI
3. Cantor B, Chang I, Knight P, Vincent A. Microstructural development in equiatomic multicomponent alloys. *Mater Sci Eng A* 2004;375-377:213-8. DOI
4. Ye Y, Wang Q, Lu J, Liu C, Yang Y. High-entropy alloy: challenges and prospects. *Mater Today* 2016;19:349-62. DOI
5. George EP, Raabe D, Ritchie RO. High-entropy alloys. *Nat Rev Mater* 2019;4:515-34. DOI
6. Naeem M, He H, Zhang F, et al. Cooperative deformation in high-entropy alloys at ultralow temperatures. *Sci Adv* 2020;6:eaax4002. DOI PubMed PMC
7. Liu D, Yu Q, Kabra S, et al. Exceptional fracture toughness of CrCoNi-based medium- and high-entropy alloys at 20 kelvin. *Science* 2022;378:978-83. DOI PubMed
8. Gludovatz B, Hohenwarter A, Catoor D, Chang EH, George EP, Ritchie RO. A fracture-resistant high-entropy alloy for cryogenic applications. *Science* 2014;345:1153-8. DOI PubMed
9. Zhang C, Yu Q, Tang YT, et al. Strong and ductile FeNiCoAl-based high-entropy alloys for cryogenic to elevated temperature multifunctional applications. *Acta Mater* 2023;242:118449. DOI
10. Han L, Maccari F, Souza Filho IR, et al. A mechanically strong and ductile soft magnet with extremely low coercivity. *Nature* 2022;608:310-6. DOI PubMed PMC
11. Yang T, Zhao YL, Tong Y, et al. Multicomponent intermetallic nanoparticles and superb mechanical behaviors of complex alloys. *Science* 2018;362:933-7. DOI PubMed
12. Ding Q, Zhang Y, Chen X, et al. Tuning element distribution, structure and properties by composition in high-entropy alloys. *Nature* 2019;574:223-7. DOI PubMed
13. Yang T, Zhao YL, Li WP, et al. Ultrahigh-strength and ductile superlattice alloys with nanoscale disordered interfaces. *Science* 2020;369:427-32. DOI PubMed
14. Zhang BB, Tang YG, Mei QS, Li XY, Lu K. Inhibiting creep in nanograined alloys with stable grain boundary networks. *Science* 2022;378:659-63. DOI PubMed
15. Wang J, Kou Z, Fu S, et al. Ultrahard BCC-AlCoCrFeNi bulk nanocrystalline high-entropy alloy formed by nanoscale diffusion-induced phase transition. *J Mater Sci Technol* 2022;115:29-39. DOI
16. Han L, Xu X, Wang L, Pyczak F, Zhou R, Liu Y. A eutectic high-entropy alloy with good high-temperature strength-plasticity balance. *Mater Res Lett* 2019;7:460-6. DOI
17. Han L, Xu X, Li Z, Liu B, Liu CT, Liu Y. A novel equiaxed eutectic high-entropy alloy with excellent mechanical properties at elevated temperatures. *Mater Res Lett* 2020;8:373-82. DOI
18. Li Z, Raabe D. Influence of compositional inhomogeneity on mechanical behavior of an interstitial dual-phase high-entropy alloy. *Mater Chem Phys* 2018;210:29-36. DOI
19. Bhattacharjee P, Sathiaraj G, Zaid M, et al. Microstructure and texture evolution during annealing of equiatomic CoCrFeMnNi high-entropy alloy. *J Alloys Compd* 2014;587:544-52. DOI
20. Zhang K, Fu Z, Zhang J, et al. Annealing on the structure and properties evolution of the CoCrFeNiCuAl high-entropy alloy. *J Alloys Compd* 2010;502:295-9. DOI
21. Kui HW, Greer AL, Turnbull D. Formation of bulk metallic glass by fluxing. *Appl Phys Lett* 1984;45:615-6. DOI

22. Utigard TA. The properties and uses of fluxes in molten aluminum processing. *JOM* 1998;50:38-43. DOI
23. Lau C, Kui H. Microstructures of undercooled germanium. *Acta Metall Mater* 1991;39:323-7. DOI
24. Ho C, Leung C, Yip Y, Mok S, Kui H. Ductile $Fe_{83}C_{17}$ alloys of ultrafine networklike microstructure. *Metall Mat Trans A* 2010;41:3443-51. DOI
25. Ho CM, Kui HW. Ductile and high strength white cast iron of ultrafine interconnected network morphology. *Metall Mat Trans A* 2011;42:3826-37. DOI
26. Lu Y, Dong Y, Guo S, et al. A promising new class of high-temperature alloys: eutectic high-entropy alloys. *Sci Rep* 2014;4:6200. DOI
27. Gao X, Lu Y, Zhang B, et al. Microstructural origins of high strength and high ductility in an $AlCoCrFeNi_{2.1}$ eutectic high-entropy alloy. *Acta Mater* 2017;141:59-66. DOI
28. Wu Z, Lu X, Wu Z, Kui H. Spinodal decomposition in $Pd_{41.25}Ni_{41.25}P_{17.5}$ bulk metallic glasses. *J Non Cryst Solids* 2014;385:40-6. DOI
29. Chen J, Kang L, Lu H, Luo P, Wang F, He L. The general purpose powder diffractometer at CSNS. *Phys Rev B Condens Matter* 2018;551:370-2. DOI
30. Allen C. Larson RBVD. General structure analysis system (GSAS) report LAUR 86-748. Los Alamos national laboratory. 2004. Available from: https://11bm.xray.aps.anl.gov/documents/GSASManual.pdf [Last accessed on 22 March 2023].
31. Lan S, Blodgett M, Kelton KF, Ma JL, Fan J, Wang X. Structural crossover in a supercooled metallic liquid and the link to a liquid-to-liquid phase transition. *Appl Phys Lett* 2016;108:211907. DOI
32. Wu X, Wang B, Rehm C, et al. Ultra-small-angle neutron scattering study on temperature-dependent precipitate evolution in $CoCrFeNiMo_{0.3}$ high entropy alloy. *Acta Mater* 2022;222:117446. DOI
33. Xu S, Li J, Cui Y, et al. Mechanical properties and deformation mechanisms of a novel austenite-martensite dual phase steel. *Int J Plast* 2020;128:102677. DOI
34. Clausen B, Lorentzen T, Bourke MA, Daymond MR. Lattice strain evolution during uniaxial tensile loading of stainless steel. *Mater Sci Eng A* 1999;259:17-24. DOI
35. Pang J, Holden T, Wright J, Mason T. The generation of intergranular strains in 309H stainless steel under uniaxial loading. *Acta Mater* 2000;48:1131-40. DOI
36. Ma L, Wang L, Nie Z, et al. Reversible deformation-induced martensitic transformation in $Al_{0.6}CoCrFeNi$ high-entropy alloy investigated by *in situ* synchrotron-based high-energy X-ray diffraction. *Acta Mater* 2017;128:12-21. DOI
37. Fu B, Yang W, Wang Y, Li L, Sun Z, Ren Y. Micromechanical behavior of TRIP-assisted multiphase steels studied with *in situ* high-energy X-ray diffraction. *Acta Mater* 2014;76:342-54. DOI
38. Warren BE. X-ray diffraction. Courier Corporation; 1990. Available from: https://scholar.google.com/scholar?cluster=15231993657912304740&hl=zh-TW&as_sdt=0,5 [Last accessed on 22 March 2023].
39. He H, Naeem M, Zhang F, et al. Stacking fault driven phase transformation in CrCoNi medium entropy alloy. *Nano Lett* 2021;21:1419-26. DOI PubMed
40. Taylor GI. Plastic strain in metals. Available from: https://cir.nii.ac.jp/crid/1573105974372618880 [Last accessed on 22 March 2023].
41. Cheng S, Stoica AD, Wang XL, et al. Deformation crossover: from nano- to mesoscale. *Phys Rev Lett* 2009;103:035502. DOI PubMed
42. Wang B, He H, Naeem M, et al. Deformation of CoCrFeNi high entropy alloy at large strain. *Scr Mater* 2018;155:54-7. DOI
43. Chen X, Wang Q, Cheng Z, et al. Direct observation of chemical short-range order in a medium-entropy alloy. *Nature* 2021;592:712-6. DOI PubMed
44. Lan S, Zhu L, Wu Z, et al. A medium-range structure motif linking amorphous and crystalline states. *Nat Mater* 2021;20:1347-52. DOI
45. Lan S, Wu Z, Wei X, et al. Structure origin of a transition of classic-to-avalanche nucleation in Zr-Cu-Al bulk metallic glasses. *Acta Mater* 2018;149:108-18. DOI
46. Li Q, Kui H. Formation of bulk magnetic nanostructured $Fe_{40}Ni_{40}P_{14}B_6$ alloys by metastable liquid state phase separation. *MRS Online Proc Lib* 1999;581:277-82. DOI
47. Cahn JW. On spinodal decomposition. *Acta Metall* 1961;9:795-801. DOI
48. Nagashio K, Kuribayashi K. Growth mechanism of twin-related and twin-free facet Si dendrites. *Acta Mater* 2005;53:3021-9. DOI
49. Schwarz M, Karma A, Eckler K, Herlach DM. Physical mechanism of grain refinement in solidification of undercooled melts. *Phys Rev Lett* 1994;73:1380-3. DOI PubMed
50. Herlach DM, Simons D, Pichon PY. Crystal growth kinetics in undercooled melts of pure Ge, Si and Ge-Si alloys. *Philos Trans A Math Phys Eng Sci* 2018;376:20170205. DOI PubMed PMC
51. Jackson K. The present state of the theory of crystal growth from the melt. *J Cryst Growth* 1974;24-25:130-6. DOI
52. Cahn JW. Theory of crystal growth and interface motion in crystalline materials. *Acta Metall* 1960;8:554-62. DOI
53. Fan J, Zhang L, Yu P, et al. A novel high-entropy alloy with a dendrite-composite microstructure and remarkable compression performance. *Scr Mater* 2019;159:18-23. DOI
54. Shi P, Ren W, Zheng T, et al. Enhanced strength-ductility synergy in ultrafine-grained eutectic high-entropy alloys by inheriting microstructural lamellae. *Nat Commun* 2019;10:489. DOI PubMed PMC
55. Wu Z, Bei H, Otto F, Pharr G, George E. Recovery, recrystallization, grain growth and phase stability of a family of FCC-structured multi-component equiatomic solid solution alloys. *Intermetallics* 2014;46:131-40. DOI

56. Senkov O, Wilks G, Scott J, Miracle D. Mechanical properties of $Nb_{25}Mo_{25}Ta_{25}W_{25}$ and $V_{20}Nb_{20}Mo_{20}Ta_{20}W_{20}$ refractory high entropy alloys. *Intermetallics* 2011;19:698-706. DOI
57. Wang Z, Baker I, Guo W, Poplawsky JD. The effect of carbon on the microstructures, mechanical properties, and deformation mechanisms of thermo-mechanically treated $Fe_{40.4}Ni_{11.3}Mn_{34.8}Al_{7.5}Cr_6$ high entropy alloys. *Acta Mater* 2017;126:346-60. DOI
58. Takeuchi A, Inoue A. Classification of bulk metallic glasses by atomic size difference. *Mater Trans* 2005;46:2817-29. DOI
59. Harjo S, Tomota Y, Lukáš P, et al. *In situ* neutron diffraction study of α-γ Fe-Cr-Ni alloys under tensile deformation. *Acta Mater* 2001;49:2471-9. DOI
60. Lee S, Woo W, De Cooman BC. Analysis of the plasticity-enhancing mechanisms in 12 pctMn Austeno-ferritic steel by *in situ* neutron diffraction. *Metall Mat Trans A* 2014;45:5823-8. DOI
61. Tomota Y, Tokuda H, Adachi Y, et al. Tensile behavior of TRIP-aided multi-phase steels studied by *in situ* neutron diffraction. *Acta Mater* 2004;52:5737-45. DOI
62. Naeem M, He H, Harjo S, et al. Temperature-dependent hardening contributions in CrFeCoNi high-entropy alloy. *Acta Mater* 2021;221:117371. DOI
63. Das A, Tarafder S. Geometry of dimples and its correlation with mechanical properties in austenitic stainless steel. *Scr Mater* 2008;59:1014-7. DOI
64. Parrington RJ. Fractography of metals and plastics. *Pract Fail Anal* 2002;2:16-9. DOI